catalysts

MDPI

Article

Facile Etching Process for the Porous Structure of Hexagonal Boron Nitride as a Catalyst Support Using Metal Oxides Under Low-Temperature Conditions

Myeung-Jin Lee [1,†], Donghyeok Kim [1,†], Nahea Kim [1], Sang-Hyeok Seo [1], Dahye Park [1], Tae-hyung Kim [2], Bora Jeong [1] and Hong-Dae Kim [1,*]

[1] Ulsan Technology Application Division, Korea Institute of Industrial Technology, Ulsan 44413, Republic of Korea; leemj@kitech.re.kr (M.-J.L.); dhkim97@kitech.re.kr (D.K.); nahea007@kitech.re.kr (N.K.); seosang0422@kitech.re.kr (S.-H.S.); dhpark67@kitech.re.kr (D.P.); bora1106@kitech.re.kr (B.J.)

[2] Department of R&D, Korea Institute of Limestone and Advanced Materials, Danyang-gun 27003, Republic of Korea; ttthkim@kilam.re.kr

* Correspondence: hdkim@kitech.re.kr; Tel.: +82-52-980-6650

† These authors contributed equally to this work.

Abstract

Many technological fields have adopted composites with active material–support configurations, where the active materials dictate the catalytic activity, and the supports improve the properties. Hexagonal boron nitride (h-BN) is a promising and highly stable support material with limited applications because it is difficult to modify. In this work, a facile method for the etching of h-BN was achieved using metal oxide (MO_X) nanoparticles. The nanoporous structure of etched h-BN was revealed by selective removal of MO_X on the surface; as a result, the specific surface area and pore volume increased more than two-fold. Then, to verify the effect of the nanoporous structure, etched h-BN was used to support the catalyst because the nanoporous structure has an advantage in dispersing the nanoparticles. Fabricated etched h-BN-added catalysts exhibited high performance in N_2O conversion. This high performance was attributed to the changed oxidation states of metal cations by interaction-etched h-BN using MO_X nanoparticles. This study serves as a basis for the development of nanocomposites with various cations and supports for catalytic reaction systems.

Keywords: hexagonal boron nitride; etching; porous structure; metal oxide; N_2O conversion

Check for updates

Academic Editor: Rui Wang

Received: 14 August 2026
Revised: 1 September 2026
Accepted: 10 September 2026
Published: 17 September 2026

Copyright: © 2026 by the authors. Licensee MDPI, Basel, Switzerland. This article is an open access article distributed under the terms and conditions of the Creative Commons Attribution (CC BY) license.

1. Introduction

The active material–support material configuration has been widely adopted for the fabrication of composites for use in various technological fields [1–4], particularly for heterogeneous catalysis [5,6], because synergistic effects between the active and support materials can enhance the physicochemical properties of the composites. Although the active materials strongly influence the overall activities of composites, the support materials play an important role in improving their properties [7,8]. Among the various requirements for support materials, the cardinal ones are high thermal and chemical stability for the firm anchoring of dispersed active materials. Hexagonal boron nitride (h-BN), a two-dimensional (2D) material, has been widely studied due to its unique properties [9,10]. In particular, h-BN exhibits excellent thermal and chemical stability, making it an attractive

support material. However, conversely, its high stability restricts the applicability of h-BN, because the inertness of highly stable materials hinders their modifiability. Therefore, the structural and chemical modification of h-BN requires large amounts of energy and harsh conditions. For example, harsh wet or plasma-etching processes, along with heat treatments at temperatures above 900 °C, are required for the fabrication of etched h-BN [11–14]. This considerably limits its application. In this study, we report a facile method for the etching of h-BN by the nucleation and growth of metal oxide nanoparticles (NPs) with low energy inputs. The composition of the formed oxide NPs can be precisely controlled. Furthermore, pores can be formed on h-BN via the selective removal of oxide NPs by acid treatment of the nanocomposites. The nanoporous structure of etched h-BN was revealed by selective removal of MO_X on the surface, resulting in the specific surface area and pore volume being increased more than two-fold. Then, to verify the effect of the nanoporous structure, etched h-BN was used to support the catalyst as its nanoporous structure has an advantage in dispersing the nanoparticles.

Greenhouse gases have been restricted as part of the net-zero scheme of the Paris Agreement adopted in the United Nations framework convention on climate change (UNFCCC, 2015) [15,16]. Among the six major greenhouse gases, nitrous oxide (N_2O) ranks as the third most significant anthropogenic gas and is emitted from various sources, such as agriculture, aquaculture, wastewater treatment, biomass burning, fossil fuel combustion, and industry [17,18]. In particular, N_2O has 310-times-higher global warming potential (GWP) than that of carbon dioxide (CO_2). Moreover, N_2O is a harmful substance in itself, but derivative problems should be solved. Stratospheric ozone is depleted by N_2O, which has a long lifespan of 114 years in the atmosphere [18–20]. Thus, N_2O emissions should be restricted, and the necessary technologies to achieve this have been researched [18,21,22]. We focused on N_2O emissions from fossil fuel combustion, from which carbon monoxide (CO) is also emitted. The generated CO is eventually oxidized to CO_2 during combustion, and the oxidation energy can be intentionally used for N_2O removal. A representative technology for this process is the selective catalytic reduction (SCR) of N_2O with CO as a reductant [23,24]. An optimum composition of catalysts was determined by screening the various candidates as transition metal oxide catalysts, and Cu-Ni-based catalysts were selected as best component. It was found that the nanoparticles were easily aggregated because the catalysts for N_2O removal were continuously used while exposed to heat [25]. To solve this problem, h-BN was not only considered to improve the dispersibility, but was also found to be suitable for enhancing the performances of catalysts, being a material with excellent chemical and thermal stability [26–28]. The improved dispersion of TMO nanoparticles was observed via transmission electron microscopy for the etched h-BN-added catalyst. The addition of h-BN increased the Cu^{2+} ratio to a level which was favorable for N_2O reduction, resulting in enhanced catalytic performances evaluated on a fixed bed. N_2O conversion of >99% was exhibited above 150 °C.

2. Results

2.1. Nanoporous Structure of Etched Hexagonal Boron Nitride

Various metals were chosen as the constituent metal elements (cations) of NPs used for etching h-BN for the following reasons. As shown in the Ellingham diagram (Figure S1), BN decomposition by the formation of metal oxide occurs at relatively low temperatures. Furthermore, vanadium- and/or copper-based oxides are promising materials for environmental catalysts [5,29–31]. The intersection in the Ellingham diagram indicates that two different reactions can occur at the same time. Because vacancies of h-BN are generated by oxidation reactions, it is possible that etching can occur at the temperature of the intersection. This was supported by the TGA results (Figure S2). The peaks of weight

loss appeared at 350 °C for W-containing nanocomposites, which were similar to those in the Ellingham diagram. For the catalytic etching of h-BN using metal-oxide NPs, the calcination temperature was selected as 350 °C based on the Ellingham diagram and results of thermogravimetric analysis (TGA) (Figures S1 and S2). Metal cations were impregnated on pristine h-BN, following which the samples were calcined, as shown in Figure 1 (for details, see Section 3), resulting in the formation of nanocomposites of metal oxide NPs and h-BN (MO_X/h-BN). In this study, pristine h-BN was catalytically etched by tungsten oxides (MO_X = WO_X), and the etched h-BN was prepared and utilized.

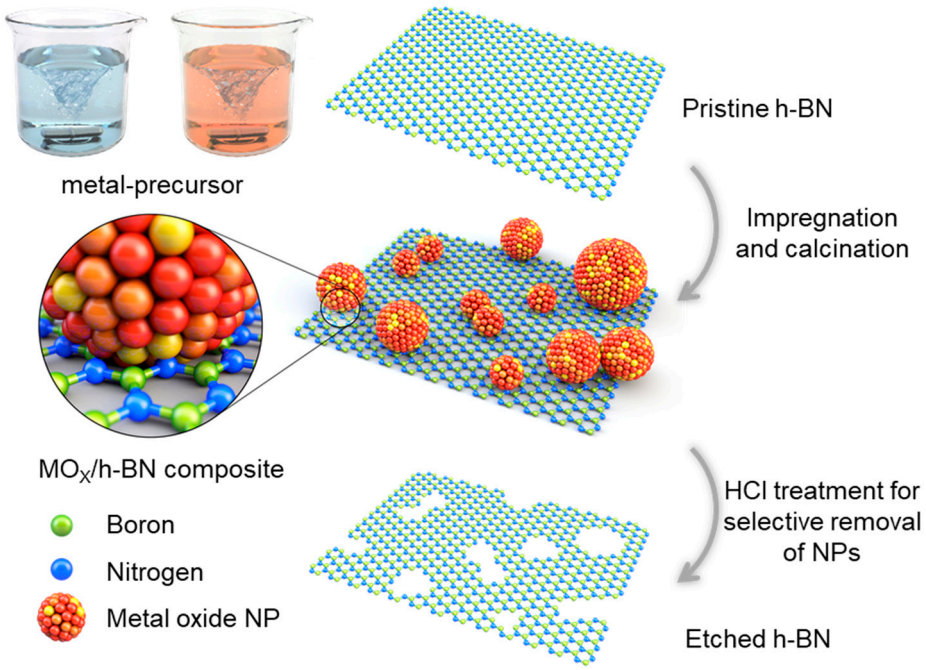


Figure 1. Schematic of the formation of etched h-BN by metal oxide and h-BN nanocomposites (MO_X/h-BN). MO_X/h-BN was prepared by impregnating metal oxide NPs onto h-BN and calcinating. Selective removal of the metal oxide NPs from MO_X/h-BN resulted in an etched h-BN structure.

Furthermore, etched h-BN sheets were obtained by the selective removal of the NPs from the nanocomposites via acid treatment, and the presence of WO_X was not observed following X-ray photoelectron spectroscopy (Figure S3). Then, the etched and carved surface was observed using scanning electron microscopy (SEM; Figure 2a), and the porous structures were observed using atomic force microscopy (AFM; Figure 2b). The measured depth and width profile showing the size of the etched area indicated the nanoporous structure on the surface of h-BN. The morphologies and crystalline nature of the samples were investigated using transmission electron microscopy (TEM; Figure 2c). The structure exhibited the lattice fringes corresponding to h-BN, with a (002) d-spacing of 3.33 Å [13]. The fast-Fourier-transform (FFT) image shows a typical hexagonal pattern for the basal plane of h-BN. The pores were also observed using TEM. Amorphous carbon films of the TEM grid were exposed through the etched area of h-BN. The (002) plane corresponds to 26.7° 2θ in the X-ray diffraction (XRD) patterns (Figure 2d, JCPDS card no. 34-0421) [32]. After etching and NP removal (denoted as etched h-BN), the relative XRD peak intensities of (100) and (101) decreased in comparison with those of the basal planes such as (002) and (004) [10].

The Fourier-transform infrared spectra (FT-IR) showed that the intensities of the signals for B–N stretching decreased (at 1370 and 817 cm^{-1}) and new B–N bending signals appeared (below 800 cm^{-1}) after etching and NP removal (Figure 2e). Dangling bond signals for B–OH, N–OH, and N–H also appeared at 1104, 1642, and 1664 cm^{-1}, respec-

tively [33]. This showed the formation of the pores because these bonds were exposed on the surface of the etched h-BN after NP removal, whereas pristine h-BN lacks these bonds. These results indicate that the B–N bond vibration modes changed from stretching to bending [9], and that more dangling bonds were generated owing to additional pore formation resulting from catalytic etching. The Brunauer–Emmett–Teller (BET)-specific surface areas for pristine h-BN and etched h-BN were 14.1 and 39.8 $m^2 \cdot g^{-1}$, respectively (Table S1). The N_2 adsorption–desorption isotherms are classified as type IV (as designated by the International Union of Pure and Applied Chemistry (IUPAC)), and the measured hysteresis loops are classified as a mixture of H1-type for cylindrical pores and H3-type for irregular pores between layers in 2D materials (Figure 2f) [34]. Moreover, the etched h-BN had larger pore volumes than the pristine h-BN when examining Barrett–Joyner–Halenda (BJH) pore distribution due to the generated porous structures (Figure 2g). Furthermore, increases in specific surface area and pore volume occurred regardless of the type of metal precursor (Figure S4).

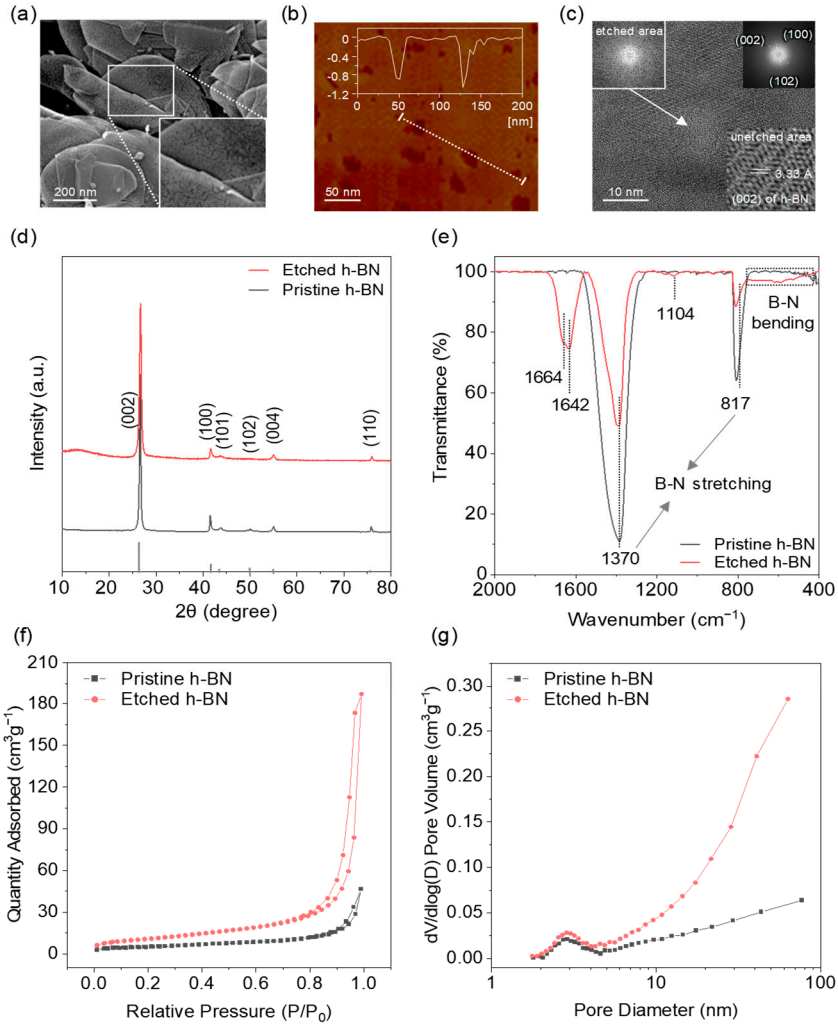


Figure 2. Characterization of the nanoporous structure of etched h-BN. (**a**) SEM image, (**b**) AFM image for etched h-BN showing the depth and width profile along the dotted line (inset), and (**c**) TEM images for porous h-B with fast-Fourier-transformation (FFT) imagery for the etched area (**upper left**); FFT image (**upper right**) and a more magnified image (**lower right**) of the unetched area. (**d**) X-ray diffraction patterns in the 2θ range from 10° to 80°, (**e**) FT-IR spectra in the wavenumber range of 2000–400 cm^{-1}, (**f**) BET hysteresis curves based on N_2-adsorption–desorption, and (**g**) BJH pore distribution of pore volume measured on BET for pristine h-BN and etched h-BN.

UV–vis measurements showed that absorption occurred at 202 nm in common h-BN, and etched h-BN showed a distinct new peak at 225 nm in comparison with pristine h-BN (Figure 3a). Through Tauc plot transformation, the etched h-BN had an energy of 5.61 eV corresponding to the band gap (E_g) and a new energy level of 4.26 eV presumed by the generated defect owing to surface etching (Figure 3b). The photoluminescence (PL) of the samples was measured via excitation using a laser at a wavelength of 213 nm. The peak at 221 nm corresponded to an E_g of 5.61 eV. The PL spectra (Figure 3c) show that after etching and selective removal of metal oxide NPs, one distinct peak appeared at 291 nm (corresponding to 4.26 eV) that corresponds to the defect levels generated by the additional B-vacancy (denoted as V_B) formations [35–37]. When a laser with a wavelength of 266 nm was used for the excitation (Figure 3d), the spectrum for etched h-BN had a peak at 501 nm (2.48 eV) corresponding to V_B and oxygen levels for the N-vacancy (denoted as O_N) [36,38]. This phenomenon was academically supported by DFT calculation, suggesting that the B-vacancy was preferentially generated on the surface of h-BN [35]. The PL spectrum (excited at 213 nm) for the metal oxides and h-BN nanocomposites without selective metal oxide NP removal (denoted as MO_X/h-BN) shows only one peak at 222 nm (5.586 eV), which corresponds to the band-gap energy of h-BN ($\leq$380 nm). Furthermore, the vacancies were generated solely by the etching process, and not acid treatment (Figure S5). The investigated XPS spectra indicated that no peak shift occurred after HCl treatment, whereas a distinct peak shift occurred for etched BN. In the case of 266 nm excitation, the relative PL peak intensity of MO_X/h-BN was lower than those of the pristine and etched h-BNs. These PL spectra suggest that the defect sites of pristine h-BN are the nucleation sites of the metal oxides, and that the etching of h-BN simultaneously occurred via the formation of the metal oxide NPs [9]. This simultaneous etching of h-BN and the formation of metal oxide NPs is in agreement with the Ellingham diagram (Figure S1).

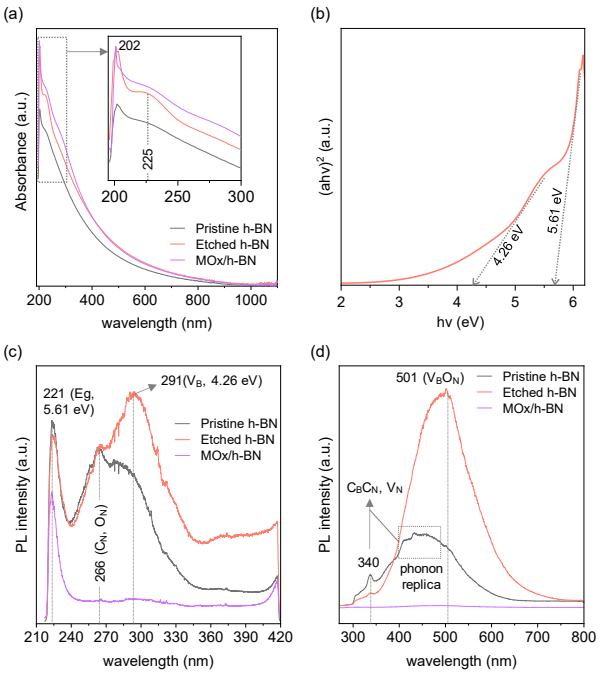


Figure 3. (**a**) Absorbance measured on UV–vis spectrum resulting in (**b**) a Tauc plot for etched h-BN. Photoluminescence (PL) spectra based on laser excitation at a wavelength of (**c**) 213 nm and (**d**) 266 nm, respectively, for pristine h-BN, etched h-BN, and nanocomposites of transition metal oxides and h-BN (MO_X/h-BN).

2.2. Catalyst for N_2O Conversion

To verify the effect of the nanoporous structure, etched h-BN was used to support the catalyst, seeing as a nanoporous structure has an advantage in dispersing nanoparticles. The morphologies and crystalline nature were observed via transmission electron microscopy (TEM). First, the nanoparticles on the support were observed, and their average diameter was 2.13 mm for Cu/TiO_2 (Figure 4a). In X-ray diffraction patterns, peaks appeared at 25.3° and 48.2°, corresponding to the (101) and (200) planes for TiO_2 (JCPDS card no. 21-1272; Figure S6), respectively. A peak assigned to the (002) plane of hexagonal boron nitride appeared at 26.8° (JCPDS card no. 34-0421). The absence of peaks assigned to CuOx indicates that nano-sized CuOx particles were highly dispersed on the TiO_2 support [39]. The presence of CuOx was observed in a high-angle annular dark-field (HAADF) image [40]. A particle on the edge of h-BN had three lattice fringes (Figure 4b). These lattice fringes corresponded to 2.10 Å for the (111) and 2.25 Å for the (200) crystallographic plane of CuO [41–43]. Moreover, *d*-spacing of 1.98 Å corresponded to the (111) crystallographic plane of NiO [44]. The simultaneous presence of both CuO and NiO on the same particle was observed in the HAADF images.

The optimum composition of the catalysts was determined by screening the various candidates as transition metal oxide catalysts (Figure S7). Especially for CuNi/TiO_2, a N_2O conversion of 61.7% was exhibited at 225 °C, and continued to increase up to 99.8% at 400 °C. The shift in T_{50} for CuNi/TiO_2 was a remarkable change in comparison to Cu-only/TiO_2 and Ni-only/TiO_2. Therefore, we selected CuNi/TiO_2 as the best component for the catalyst; thereafter, catalysts were synthesized with various contents of Cu and Ni (Figure 4c). T_{50} appeared at the following temperatures: 175 °C (for 3Cu7Ni/TiO_2), 225 °C (for 5Cu5Ni/TiO_2), 250 °C (for 7Cu3Ni/TiO_2), and 400 °C (for 1Cu9Ni/TiO_2, Cu-only/TiO_2, and Ni-only/TiO_2). Among them, 3Cu7Ni/TiO_2 (S_{BET} of 71.86 $m^2 \cdot g^{-1}$; Table S2), which exhibited the highest efficiencies in N_2O conversion over all evaluation temperatures, achieved 75.2% at 175 °C and 100% at 400 °C, owing to the lowest activation energy (E_a) of 31.75 $kJ \cdot mol^{-1}$ (Figure 4d). 3Cu7Ni/TiO_2 with the addition of pristine h-BN (S_{BET} of 63.78 $m^2 \cdot g^{-1}$) exhibited improved N_2O conversion, while the etched h-BN-added catalyst (S_{BET} of 78.19 $m^2 \cdot g^{-1}$) exhibited a further increased N_2O conversion of 93.5% and N_2 selectivity of ~100% at 125 °C (Figures 4e and S8a). In a comparison of 3Cu7Ni/TiO_2 with/without pristine BN, the increased performances indicated the chemical influence of TiO_2 support dilution and BN composition. Furthermore, for catalysts with pristine BN and/or etched BN, the results show the structural influence of porosity. The catalyst durability and improved performances on etched-BN incorporation were confirmed by the results of a consistent N_2O conversion over ~99% for 10 h in long-term tests (Figure 4f), with the turnover frequency value calculated at 0.823 h^{-1} (Figure 4g). The results of the blank test for pristine BN and etched BN without active metal oxides indicated that prepared h-BN only served sites with dispersed active materials as a support for catalysts (Figure S8b,c).

Cu- and/or Ni-contained catalysts were investigated using X-ray photoelectron spectroscopy to determine the oxidation states of transition metal oxides. The deconvoluted XPS narrow scan spectra of Cu 2p and Ni 2p were shown in Figure 4h,i, and the quantitatively calculated value was displayed in Figure 4j. Copper exists in various oxidation states, which appeared as Cu^{2+} $2p_{1/2}$ (954.11–953.50 eV), Cu^{1+} $2p_{1/2}$ (952.21–950.89 eV), Cu^{2+} $2p_{3/2}$ (932.54–932.52 eV), and Cu^{1+} $2p_{3/2}$ (931.79–931.08 eV) [45]. For 3Cu7Ni/TiO_2, the presence of Cu^{2+} was not observed. Here, the ratio of Cu^{2+} increased to 37.16% for catalysts with pristine h-BN, and it further increased up to 56.26% following the addition of etched h-BN. Among these oxidation states, Cu^{2+} has the most preferable redox ability for N_2O conversion [46]. In the case of Ni 2p, three species appeared as satel-

lites, namely Ni^{3+}, Ni^{2+}, and $Ni^{\delta+}$. Among them, Ni^{3+} 2p1/2 appeared in a range of 874.83–873.64 eV, and 856.45–856.27 eV for Ni^{3+} 2p3/2 [47,48]. Regardless of the other components, the Ni-containing catalyst exhibited similar Ni^{3+} ratios. Ni^{2+} appeared in a range of 872.95–872.22 eV for Ni^{2+} 2p1/2, while appearing in a range of 855.21–855.04 eV for Ni^{2+} 2p3/2. For $3Cu7Ni/TiO_2$, the ratio of Ni^{2+} was calculated as 26.77%, and this increased to 31.05% for $3Cu7Ni/TiO_2$ with the addition of pristine h-BN. The addition of etched h-BN further increased the Ni^{2+} ratio up to 35.88%. The high Ni^{2+} ratio also positively assisted the electron transfer of Cu^{2+} during N_2O conversion.

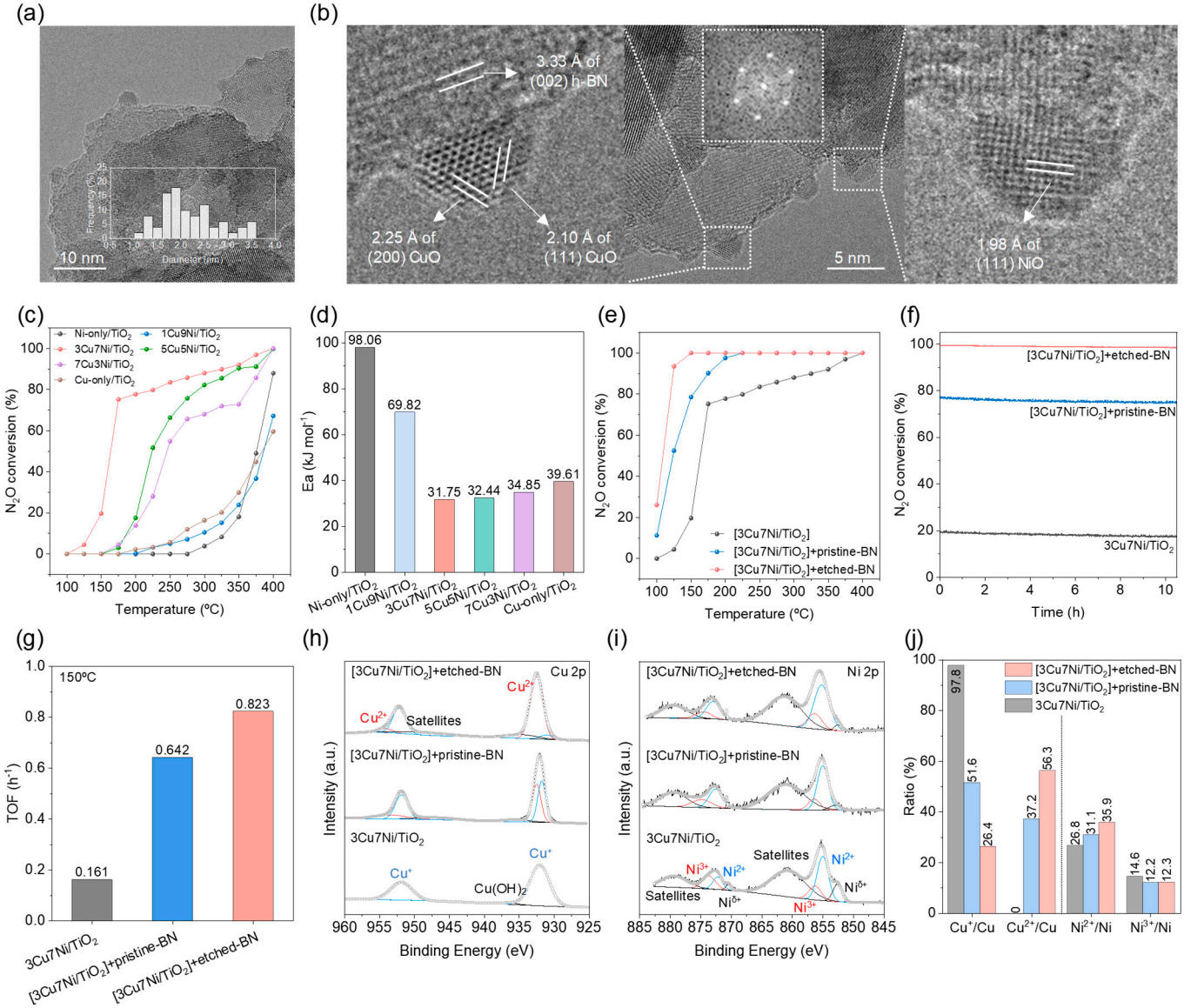


Figure 4. (**a**) Morphologies of $3Cu7Ni/TiO_2$ with etched h-BN catalyst from the scanning-TEM (STEM) images with particle size histogram (inset), and (**b**) high-resolution image with fast Fourier transformation (FFT; inset). (**c**) N_2O conversion of $3Cu7Ni/TiO_2$ catalyst series with various components under gaseous conditions of $[N_2O]$ = 180 ppm, [CO] = 540 ppm, $[N_2]$ = balance, and GHSV = 60,000 h^{-1} over the temperature range of 100–400 °C, and (**d**) calculated activation energy for N_2O conversion reaction. (**e**) N_2O conversion under the same gaseous conditions with (**c**) for $3Cu7Ni/TiO_2$ catalyst with/without pristine h-BN and etched h-BN. (**f**) Long-term stability tests and (**g**) calculated turnover frequencies at 150 °C. Deconvoluted (**h**) Cu 2p and (**i**) Ni 2p spectra of X-ray photoelectron spectroscopy resulting in (**j**) the calculated ratio of oxidation states for the $3Cu7Ni/TiO_2$ catalyst with/without pristine h-BN and etched h-BN.

Catalytic reducibility could be inferred from hydrogen-temperature-programmed-reduction (H_2-TPR) profiles of the synthesized catalysts over the temperature range of 100–500 °C (Figure S9a). For Cu-only/TiO_2, peaks appeared at 161, 196, and 354 °C, which corresponded to Cu_α (assigned to dispersed CuO species), Cu_β (assigned to CuO-support species), and Cu_δ (assigned to bulk CuO species), respectively [49–51]. The temperature of the Cu_α peak shifted from 161 °C to 140 °C for 3Cu7Ni/TiO_2 and 3Cu7Ni/TiO_2 with the addition of etched h-BN, along with the disappearance of Cu_δ. The amount of H_2 consumption increased from 0.43 to 0.61 mmol·g^{-1} by comparing Cu-only/TiO_2 with 3Cu7Ni/TiO_2, and it further increased up to 0.84 mmol·g^{-1} by the addition of h-BN (Table S3). The shift in temperature vertex and increased H_2 consumption indicates that the reduction in dispersed CuO species was largely driven by the low energy input. In the case of Ni-only/TiO_2, a peak at 300 °C was deconvoluted as three species. Ni_α species resulted from the reduction from Ni^{3+} to Ni^{2+} of Ni_2O_3, and Ni_β species appeared following the interaction between NiO and TiO_2 support. Ni_γ corresponded to the reduction from Ni^{2+} to Ni^0 of NiO [52,53]. The total amount of H_2 consumption for Ni species increased from 1.07 to 1.32 mmol·g^{-1} following the addition of Cu, which was 1.29 mmol·g^{-1} for 3Cu7Ni/TiO_2 with etched h-BN. Among the various Ni species, the amounts of H_2 consumption for Ni_β decreased from 0.63 to 0.34 mmol·g^{-1} following the addition of Cu and h-BN, and this increased from 0.19 to 0.32 for Cu_γ. These results indicated that NiO interactions with TiO_2 support affected NiO interactions with the dispersed CuO species (denoted as Cu_α), and the addition of etched h-BN enhanced the interaction between NiO and CuO. The increased ratios of Cu^{2+} and Ni^{2+} were in agreement with the XPS results. In the Cu-Ni system, the high ratios of Cu^{2+} and Ni^{2+} were the main factors, because the redox reaction occurred from Cu^{2+}–Ni^{2+} to Cu^{1+}–Ni^{3+} for N_2O conversion [54,55]. Also, the low energy input for the reduction indicated an easy electron transfer; this excellent reducibility enhanced the N_2O decomposition performances.

CO-temperature-programmed-desorption (CO-TPD) profiles of the catalyst were investigated to observe the behaviors of CO on the catalysts over a temperature range of 50–800 °C (Figure S9b). The amount of CO desorption for Cu/TiO_2 was calculated as 0.69 mmol·g^{-1} and 0.91 for Ni-only/TiO_2 (Table S4). The CO-adsorption capacity of Ni-only/TiO_2 was more favorable than that of Cu-only/TiO_2. Although the amounts of CO desorption decreased to 0.67 mmol·g^{-1} for 3Cu7Ni/TiO_2, those recovered up to 0.89 with the addition of etched h-BN. The adsorption/desorption behaviors of CO were more active on the surface of NiO than CuO; thus, the levels of CO desorption decreased in the mixed system of Cu-Ni when comparing Ni-only/TiO_2. The activities of CO adsorption/desorption recovered because the NiO nanoparticles were highly dispersed by the addition of etched h-BN. In particular, peaks at relatively low temperatures were assigned CO desorption from highly dispersed NiO nanoparticles, while those at relatively high temperatures were assigned desorption from terrace sites [56]. Therefore, for 3Cu7Ni/TiO_2 with etched h-BN, the largest amounts of CO desorption were caused by the improved dispersion of NiO nanoparticles on the surface of h-BN and TiO_2. Fourier-transform infrared (FT-IR) spectra were investigated in a range of 2000–800 cm^{-1} for the catalysts (Figure S9c). For 3Cu7Ni/TiO_2 with etched h-BN, a peak at 1401 cm^{-1} corresponded to in-plane stretching vibrations of the B–N bond, and out-of-plane vibrations of the B–N–B bond appeared at 817 cm^{-1} [57]. Also, peaks at 1113 and 1043 cm^{-1} were found corresponding to M–OH and M–O–M, respectively, and transmittances of those peaks was highest for 3Cu7Ni/TiO_2 with etched h-BN [58]. The highest intensities indicated that more transition metal oxide nanoparticles were exposed than for the other catalysts.

3. Materials and Methods

3.1. Materials

All solid reagents except titanium dioxide powder (TiO_2, >85%, NANO Co., Ltd., Sangju, Republic of Korea) were purchased from Sigma-Aldrich (St. Louis, MO, USA): hexagonal boron nitride powder (h-BN, 98%); ammonium metavanadate (NH_4VO_3, 99.95%); ammonium metatungstate hydrate ($(NH_4)_6[H_2W_{12}O_{40}]\cdot nH_2O$, 99.99%); copper(II) nitrate trihydrate ($Cu(NO_3)_2\cdot 3H_2O$, 99.9%); nickel(II) nitrate hexahydrate ($Ni(NO_3)_2\cdot 6H_2O$, 98.5%); cobalt(II) nitrate hexahydrate ($Co(NO_3)_2\cdot 6H_2O$, 98%); manganese(II) nitrate tetrahydrate ($Mn(NO_3)_2\cdot 4H_2O$, 99.99%); and cerium nitrate hexahydrate ($Ce(NO_3)_2\cdot 6H_2O$, 98%). Anhydrous ethanol (C_2H_5OH, 99.9%, hydrochloric acid (HCl, 35%), and ammonia hydroxide (NH_4OH, 30%) were purchased from Daejung Chemicals and Metals Co., Ltd. (Siheung, Republic of Korea). All the reagents were used without further purification.

3.2. Etched h-BN from Nanocomposites of Metal Oxides and h-BN (MO_X/h-BN)

First, the metal precursors were dissolved in anhydrous ethanol. Similarly, h-BN powders were dispersed in anhydrous ethanol by sonication for 1 h. Thereafter, the metal precursor solution and the h-BN suspension were mixed under stirring for 1 h. The mixed suspension was dried at 60 °C in an oil bath and the obtained powder was ground. Finally, the metal oxide and h-BN nanocomposites (MO_X/h-BN) were availed by stepwise calcination of the ground powder at 350 and 400 °C for 3 and 5 h, respectively. The obtained MO_X/h-BN powder was dispersed and stirred for 30 min in hydrochloric acid (reagent as is, without dilution) for the selective removal of metal oxide NPs. A white powder was obtained upon filtering and washing in distilled water three times. The final etched h-BN was availed by drying the powder at 60 °C overnight.

3.3. Catalyst for N_2O Decomposition

The metal precursor (M = Cu, Ni, Mn, Co, and/or Nb) was dissolved in anhydrous ethanol. TiO_2 and/or h-BN (pristine or etched h-BN) were dispersed by sonication for 30 min. Thereafter, the transition metal precursor solution and the TiO_2 powder suspension were mixed under stirring for 1 h, and ammonia hydroxide was added to reach pH 10 for the mixed suspension. Dried powder was obtained by the evaporation method in an oil bath at 60 °C. The ground powder was calcined at 400 °C for 5 h. The synthesized catalyst powder was named MO_X/TiO_2, which contained approximately 10 wt.% of metal oxides in the total catalyst (hereafter M_1/TiO_2). In the case of a two-component system catalyst, the metal oxide content was 5 wt.% in the total catalyst (hereafter M_1M_2/TiO_2). Also, the added h-BN catalyst replaced 10 wt.% of TiO_2 (hereafter M_1M_2/TiO_2 with pristine h-BN or etched h-BN).

3.4. Characterization

The morphologies were observed using scanning electron microscopy (SEM; SU8000, Hitachi, Tokyo, Japan), transmission electron microscopy (TEM; JEM-2100, JEOL Ltd., Tokyo, Japan), and atomic force microscopy (AFM; Park XE100, Parks Systems, Gwacheon, Republic of Korea). The structural properties of the samples were confirmed using X-ray diffraction (XRD) patterns measured on an Ultima IV (Rigaku, Tokyo, Japan) with Cu Kα radiation (λ = 1.5406 Å) in the 2θ range 10–80° at a scan rate of 3° per minute. Brunauer–Emmet–Teller (BET) surface area, pore volume, and pore diameter of the obtained samples were measured on an ASAP 2023 (Micromeritics Instrument Crop, Norcross, GA, USA) with flowing N_2 gas after a degassing pretreatment at 150 °C for 4 h. Fourier-transform infrared spectroscopy (FT-IR) analysis was performed on a Vertex 80v (Bruker, Billerica, MA, USA) to investigate the acid sites of the samples. Attenuated total reflectance (ATR)

was conducted in the range of 4000–400 cm^{-1}, with 256 scan times, using pellets composed of 0.16 g KBr and 0.001 g of the sample. The defect levels were investigated by measuring photoluminescence (PL) with 213 nm and 266 nm excitation lasers (F-7000, Hitachi, Tokyo, Japan). The various chemical states of the samples were scanned using X-ray photoelectron spectroscopy (XPS) on a K Alpha$^+$ (Thermo VG Scientific, Waltham, MA, USA) with an Al Kα radiation source and a 0.1 eV energy step size. The samples were prepared by pre-treating those in a vacuum oven at 60 °C for 24 h to avoid moisture interference. NH_3-temperature-programmed desorption (NH_3-TPD) was performed to determine the number of acid sites by desorbing NH_3 using an AutoChem II 2920 instrument (Micromeritics Instrument Crop, Norcross, GA, USA). For NH_3-TPD, the samples were pretreated in N_2 gas at 150 °C for 4 h, and then NH_3 was adsorbed by passing 10% NH_3/He gas at 150 °C for 1 h. Then, NH_3-TPD was investigated during the temperature increase from 100 to 600 °C. Using the same equipment, H_2-temperature-programmed reduction (H_2-TPR) was also carried out to confirm the reduction ability by passing 10% H_2/Ar gas at temperatures in the range of 100–600 °C.

3.5. Catalytic Activity Test

Catalytic activity was tested on a fixed bed under the following gas conditions: 180 ppm of N_2O, 540 ppm of CO, and 2% (v/v) of O_2 (when used). N_2 was used to maintain the total flow rate of 500 $mL{\cdot}min^{-1}$. All gases were precisely regulated using a mass flow controller (MFC, 5850E, Hatfield, PA, USA) The concentrations of the gases were detected using a CX-4000 (Gasmet Technologies Oy, Vantaa, Finland) and O_2-analyzer (Oxitech-5000, Enotech, Dieburg, Germany). After the bypassed gas stream was stable, it was passed through the reactor. The synthesized catalysts were tested under a gas hourly space velocity (GHSV) of 60,000 h^{-1}. N_2O conversion, N_2 selectivity efficiency, and turnover frequency were calculated using Equations (1)–(3):

$$N_2O \text{ conversion } (\%) = \frac{[N_2O]_{in} - [N_2O]_{out}}{[N_2O]_{in}} \times 100 \quad (1)$$

$$N_2 \text{ selectivity } (\%) = \frac{[N_2O]_{in} - [N_2O]_{out} - \left[NO_{x(=1,2)}\right]_{out}}{[N_2O]_{in} - [N_2O]_{out}} \times 100 \quad (2)$$

$$TOF\ (h^{-1}) = \frac{(F_{N_2O}) \times (N_2O \text{ conversion}) \times (N_2 \text{ selectivity})}{(R) \times (T) \times (mol_{Cu})} \times 100 \quad (3)$$

4. Conclusions

Herein, we report the catalytic etching of h-BN via the formation of metal oxide NPs on h-BN. Furthermore, etched h-BN was also obtained via selective removal of the NPs formed on h-BN, demonstrating that structural modifications of high-stability materials such as h-BN can be achieved with a low energy input using catalytic etching. This facile method indicated versatility by verifying the possibility of using various metal precursors. The nanoporous structure of etched h-BN was visually observed via microscope, and the specific surface area increased from 14.1 to 39.8 $m^2{\cdot}g^{-1}$ with a large pore volume. Also, the results of optical spectroscopy indicated that the new defect level was generated due to B-vacancies. In particular, the relative PL peak intensity of MO_X/h-BN hardly appeared in comparison with the pristine and etched h-BNs. These PL spectra suggest that the defect sites of pristine h-BN can be the nucleation sites of the metal oxides, and that the etching of h-BN simultaneously occurred via the formation of the metal oxide NPs. The etched h-BN was used to support the catalyst because its nanoporous structure has an advantage in dispersing the nanoparticles. The catalyst containing etched h-BN exhibited a high

N_2O conversion performance over a wide temperature range of 150–400 °C. XPS results indicated that the high catalytic performance of 3Cu7Ni/TiO_2 with etched h-BN can be attributed to using the highest ratio of Cu^{2+}. It is expected that other transition metal oxides, in addition to the metal oxides demonstrated in this study, could also be formed on h-BN or other 2D materials using our method. Therefore, nanocomposites with many compositional and structural degrees of freedom can be used for diverse catalytic reaction systems. Furthermore, nanoporous pure h-BN sheets prepared by selective NP removal from nanocomposites can be utilized in various technological fields.

Supplementary Materials: The following supporting information can be downloaded at: https://www.mdpi.com/article/10.3390/catal16090837/s1, Figure S1. Ellingham diagram for oxidation reactions of boron nitride (BN) and several metal cation. Figure S2. TGA results for (a) W-only/h-BN, (b) pristine h-BN, and (c) precursors of tungsten (AMT). Figure S3. W 4f spectra of X-ray photoelectron spectroscopy to observe the removal of WOx (metal oxides) through HCl treatment. Figure S4. (a) BET hysteresis curves based on N_2–adsorption–desorption and (b) BJH pore distributions for pristine h-BN and etched h-BN by the several metal cation. Figure S5. (a) B 1s and (b) N 1s spectra of X-ray photoelectron spectroscopy. Figure S6. X-ray diffraction patterns of CuNi/TiO_2 with etched h-BN catalyst. Figure S7. N_2O conversion for (a) one-component and (b) two-components catalyst under gas conditions of [N_2O] = 180 ppm, [CO] = 540 ppm, [N_2] = balance, and GHSV = 60,000 h^{-1} over the temperature range of 100–400 °C. Figure S8. (a) N_2 selectivity and N_2O conversion by (b) various GHSV and (c) blank test with only h-BN. Figure S9. (a) Hydrogen-temperature-programmed-reduction (H_2-TPR) profiles, (b) CO-temperature-programmed-desorption (CO-TPD) profiles, and (c) investigated FT-IR spectra for Cu-only/TiO_2, Ni-only/TiO_2, CuNi/TiO_2, and CuNi/BN-TiO_2. Table S1. Textural properties. Specific surface area (S_{BET}), pore diameter (D_P), and pore volume (V_P) for pristine h-BN and etched h-BN by the several metal cation. Table S2. Textural properties for 3Cu7Ni/TiO_2 with/without pristine h-BN and etched h-BN. Table S3. Calculated amounts of H_2-consumption for Cu-only/TiO_2, Ni-only/TiO_2, Cu-Ni/TiO_2, and Cu-Ni/BN-TiO_2. Table S4. Calculated amounts of CO-consumption for Cu-only/TiO_2, Ni-only/TiO_2, Cu-Ni/TiO_2, and Cu-Ni/BN-TiO_2.

Author Contributions: M.-J.L. and D.K.: Conceptualization, Investigation, Methodology, Data curation, Writing—Original Draft, Writing—Review and Editing. N.K.: Methodology, Investigation. S.-H.S.: Formal Analysis, Investigation. D.P.: Formal Analysis, Investigation. T.-h.K.: Formal Analysis, Investigation. B.J.: Funding acquisition, Validation. H.-D.K.: Conceptualization, Funding acquisition, Supervision, Writing—Review and Editing. All authors have read and agreed to the published version of the manuscript.

Funding: This research was financially supported by the Ministry of Trade, Industry and Energy (MOTIE; grant number RS-2024-00432416).

Data Availability Statement: The original contributions presented in this study are included in the article and/or Supplementary Materials. Any further inquiries regarding the data may be directed to the corresponding author.

Conflicts of Interest: The authors declare no conflict of interest.

Abbreviations

The following abbreviations are used in this manuscript:

UNFCCC	united nations framework convention on climate change
GWP	global warming potential
SCR	selective catalytic reduction
TEM	transmission electron microscopy
AFM	atomic force microscopy
XRD	X-ray diffraction
BET	Brunauer–Emmet–Teller

FT-IR	Fourier-transform infrared spectroscopy
ATR	Attenuated total reflectance
PL	photoluminescence
XPS	X-ray photoelectron spectroscopy
NH_3-TPD	NH_3-temperature-programmed desorption
H_2-TPR	H_2-temperature-programmed reduction
MFC	mass flow controller
GHSV	gas hourly space velocity
TGA	thermogravimetric analysis
FFT	fast Fourier transform
IUPAC	International Union of Pure and Applied Chemistry
BJH	Barrett–Joyner–Halenda
HAADF	high-angle annular dark-field

References

1. Vayssilov, G.N.; Lykhach, Y.; Migani, A.; Staudt, T.; Petrova, G.P.; Tsud, N.; Skála, T.; Bruix, A.; Illas, F.; Prince, K.C.; et al. Support nanostructure boosts oxygen transfer to catalytically active platinum nanoparticles. *Nat. Mater.* **2011**, *10*, 310–315. [CrossRef] [PubMed]
2. Schmuch, R.; Wagner, R.; Hörpel, G.; Placke, T.; Winter, M. Performance and cost of materials for lithium-based rechargeable automotive batteries. *Nat. Energy* **2018**, *3*, 267–278. [CrossRef]
3. Vantomme, G.; Meijer, E.W. The construction of supramolecular systems. *Science* **2019**, *363*, 1396–1397. [CrossRef] [PubMed]
4. Kim, J.; Lee, M.-J.; Kim, J.; Jang, W.; Lee, J.H.; Ding, X.; Zhang, K.H.L.; An, K.; Kim, H.-D.; Cho, S. Nanoscale Precursor Distribution by Microfluidization for Scalable Production of Highly Efficient Thermocatalysts. *Adv. Funct. Mater.* **2024**, *34*, 2400341–2400352. [CrossRef]
5. Inomata, Y.; Kubota, H.; Hata, S.; Kiyonaga, E.; Morita, K.; Yoshida, K.; Sakaguchi, N.; Toyao, T.; Shimizu, K.-I.; Ishikawa, S.; et al. Bulk tungsten-substituted vanadium oxide for low-temperature NO_x removal in the presence of water. *Nat. Commun.* **2021**, *12*, 557. [CrossRef] [PubMed]
6. Shukla, P.; Wang, S.; Singh, K.; Ang, H.M.; Tadé, M.O. Cobalt exchanged zeolites for heterogeneous catalytic oxidation of phenol in the presence of peroxymonosulphate. *Appl. Catal. B Environ.* **2010**, *99*, 163–169. [CrossRef]
7. Shi, P.; Su, R.; Wan, F.; Zhu, M.; Li, D.; Xu, S. Co_3O_4 nanocrystals on graphene oxide as a synergistic catalyst for degradation of Orange II in water by advanced oxidation technology based on sulfate radicals. *Appl. Catal. B Environ.* **2012**, *123–124*, 265–272. [CrossRef]
8. Zhang, D.; Zhang, L.; Shi, L.; Fang, C.; Li, H.; Gao, R.; Huang, L.; Zhang, J. In situ supported MnO_x–CeO_x on carbon nanotubes for the low-temperature selective catalytic reduction of NO with NH_3. *Nanoscale* **2013**, *5*, 1127–1136. [CrossRef] [PubMed]
9. Zhu, W.; Wu, Z.; Foo, G.S.; Gao, X.; Zhou, M.; Liu, B.; Veith, G.M.; Wu, P.; Browning, K.L.; Lee, H.N.; et al. Taming interfacial electronic properties of platinum nanoparticles on vacancy-abundant boron nitride nanosheets for enhanced catalysis. *Nat. Commun.* **2017**, *8*, 15291. [CrossRef] [PubMed]
10. Wang, H.S.; Chen, L.; Elibol, K.; He, L.; Wang, H.; Chen, C.; Jiang, C.; Li, C.; Wu, T.; Cong, C.X.; et al. Towards chirality control of graphene nanoribbons embedded in hexagonal boron nitride. *Nat. Mater.* **2021**, *20*, 202–207. [CrossRef] [PubMed]
11. Zhang, C.; Zhao, S.; Jin, C.; Koh, A.L.; Zhou, Y.; Xu, W.; Li, Q.; Xiong, Q.; Peng, H.; Liu, Z. Direct growth of large-area graphene and boron nitride heterostructures by a co-segregation method. *Nat. Commun.* **2015**, *6*, 6519. [CrossRef] [PubMed]
12. He, Z.; Kim, C.; Lin, L.; Jeon, T.H.; Lin, S.; Wang, X.; Choi, W. Formation of heterostructures via direct growth CN on h-BN porous nanosheets for metal-free photocatalysis. *Nano Energy* **2017**, *42*, 58–68. [CrossRef]
13. Liu, Q.; Chen, C.; Du, M.; Wu, Y.; Ren, C.; Ding, K.; Song, M.; Huang, C. Porous Hexagonal Boron Nitride Sheets: Effect of Hydroxyl and Secondary Amino Groups on Photocatalytic Hydrogen Evolution. *ACS Appl. Nano Mater.* **2018**, *1*, 4566–4575. [CrossRef]
14. Li, T.; Yi, D.; Hu, J.; Xu, J.; Liu, J.; Wang, B. Surface modification of h-BN and its influence on the mechanical properties of $CuSn_{10}$/h-BN composites. *J. Alloys Compd.* **2017**, *723*, 345–353. [CrossRef]
15. King, A.D.; Peel, J.; Ziehn, T.; Bowen, K.J.; McClelland, H.L.O.; McMichael, C.; Nicholls, Z.R.J.; Sniderman, J.M.K. Preparing for a post-net-zero world. *Nat. Clim. Change* **2022**, *12*, 775–777. [CrossRef]
16. Rogelj, J.; Geden, O.; Cowie, A.; Reisinger, A. Net-zero emissions targets are vague: Three ways to fix. *Nature* **2021**, *591*, 365–368. [CrossRef] [PubMed]
17. Li, L.; Xu, J.; Hu, J.; Han, J. Reducing nitrous oxide emissions to mitigate climate change and protect the ozone layer. *Environ. Sci. Technol.* **2014**, *48*, 5290–5297. [CrossRef] [PubMed]

18. Konsolakis, M. Recent advances on nitrous oxide (N_2O) decomposition over non-noble-metal oxide catalysts: Catalytic performance, mechanistic considerations, and surface chemistry aspects. *ACS Catal.* **2015**, *5*, 6397–6421. [CrossRef]
19. Ravishankara, A.R.; Daniel, J.S.; Portmann, R.W. Nitrous oxide (N_2O): The dominant ozone-depleting substance emitted in the 21st century. *Science* **2009**, *326*, 123–125. [CrossRef] [PubMed]
20. Zaman, M.; Nguyen, M.L.; Šimek, M.; Nawaz, S.; Khan, M.J.; Babar, M.N.; Zaman, S. Emissions of nitrous oxide (N_2O) and di-nitrogen (N_2) from the agricultural landscapes, sources, sinks, and factors affecting N_2O and N_2 ratios. In *Greenhouse Gases-Emission, Measurement and Management*; IntechOpen: Rijeka, Croatia, 2012.
21. Dandekar, A.; Vannice, M.A. Decomposition and reduction of N_2O over copper catalysts. *Appl. Catal. B Environ.* **1999**, *22*, 179–200. [CrossRef]
22. Zhou, H.; Huang, Z.; Sun, C.; Qin, F.; Xiong, D.; Shen, W.; Xu, H. Catalytic decomposition of N_2O over $Cu_xCe_{1-x}O_y$ mixed oxides. *Appl. Catal. B Environ.* **2012**, *125*, 492–498. [CrossRef]
23. Chang, K.S.; Lee, H.-J.; Park, Y.-S.; Woo, J.-W. Enhanced performances of N_2O destruction in the presence of CO over the mixed metal oxide catalysts derived from hydrotalcite-type precursors. *Appl. Catal. A Gen.* **2006**, *309*, 129–138. [CrossRef]
24. Sun, R.; Yu, F.; Wan, Y.; Pan, K.; Li, W.; Zhao, H.; Dan, J.; Dai, B. Reducing N_2O formation over CO-SCR systems with CuCe mixed metal oxides. *ChemCatChem* **2021**, *13*, 2709–2718. [CrossRef]
25. Smith, S.J.; Huang, B.; Liu, S.; Liu, Q.; Olsen, R.E.; Boerio-Goates, J.; Woodfield, B.F. Synthesis of metal oxide nanoparticles via a robust "solvent-deficient" method. *Nanoscale* **2015**, *7*, 144–156. [CrossRef] [PubMed]
26. Huang, C.; Ye, W.; Liu, Q.; Qiu, X. Dispersed Cu_2O octahedrons on h-BN nanosheets for p-nitrophenol reduction. *ACS Appl. Mater. Interfaces* **2014**, *6*, 14469–14476. [CrossRef] [PubMed]
27. Lee, M.-j.; Kim, D.-H.; Lee, M.; Ye, B.; Jeong, B.; Lee, D.; Kim, H.-D.; Lee, H. Enhanced NO_x removal efficiency for SCR catalyst of well-dispersed Mn-Ce nanoparticles on hexagonal boron nitride. *Environ. Sci. Pollut. Res.* **2019**, *26*, 36107–36116. [CrossRef] [PubMed]
28. Lee, M.-j.; Ye, B.; Jeong, B.; Chun, S.-y.; Kim, T.; Kim, D.-H.; Lee, H.; Kim, H.-D. MnO_x–CeO_x Nanoparticles Supported on Porous Hexagonal Boron Nitride Nanoflakes for Selective Catalytic Reduction of Nitrogen Oxides. *ACS Appl. Nano Mater.* **2020**, *3*, 11254–11265. [CrossRef]
29. Lee, K.J.; Kumar, P.A.; Maqbool, M.S.; Rao, K.N.; Song, K.H.; Ha, H.P. Ceria added Sb-V_2O_5/TiO_2 catalysts for low temperature NH_3 SCR: Physico-chemical properties and catalytic activity. *Appl. Catal. B Environ.* **2013**, *142–143*, 705–717. [CrossRef]
30. Byun, S.W.; Lee, S.J.; Kim, M.; Bae, W.B.; Shin, H.; Hazlett, M.J.; Kang, D.; Tesfaye, B.; Park, P.W.; Kang, S.B. High N_2 selectivity of Pt-V-W/TiO_2 oxidation catalyst for simultaneous control of NH_3 and CO emissions. *Chem. Eng. J.* **2022**, *444*, 136517. [CrossRef]
31. Ek, M.; Ramasse, Q.M.; Arnarson, L.; Georg Moses, P.; Helveg, S. Visualizing atomic-scale redox dynamics in vanadium oxide-based catalysts. *Nat. Commun.* **2017**, *8*, 305. [CrossRef] [PubMed]
32. Lee, M.-J.; Jeong, B.; Kim, D.; Kim, S.-J.; Choi, Y.; Ye, B.; Kim, D.-H.; Kim, H.-D.; Cho, S. Hexagonal boron nitride heterostructure to control the oxidation states and SO_2 resistance of the V_2O_5-WO_3/TiO_2 catalyst for the NH_3-SCR reaction across a wide temperature range. *Appl. Catal. B Environ.* **2025**, *378*, 125583. [CrossRef]
33. Sudeep, P.M.; Vinod, S.; Ozden, S.; Sruthi, R.; Kukovecz, A.; Konya, Z.; Vajtai, R.; Anantharaman, M.R.; Ajayan, P.M.; Narayanan, T.N. Functionalized boron nitride porous solids. *RSC Adv.* **2015**, *5*, 93964–93968. [CrossRef]
34. Li, Y.; Wan, Y.; Li, Y.; Zhan, S.; Guan, Q.; Tian, Y. Low-Temperature Selective Catalytic Reduction of NO with NH_3 over Mn_2O_3-Doped Fe_2O_3 Hexagonal Microsheets. *ACS Appl. Mater. Interfaces* **2016**, *8*, 5224–5233. [CrossRef] [PubMed]
35. Kim, D.H.; Kim, H.S.; Song, M.W.; Lee, S.; Lee, S.Y. Geometric and electronic structures of monolayer hexagonal boron nitride with multi-vacancy. *Nano Converg.* **2017**, *4*, 13. [CrossRef] [PubMed]
36. Tran, T.T.; Bray, K.; Ford, M.J.; Toth, M.; Aharonovich, I. Quantum emission from hexagonal boron nitride monolayers. *Nat. Nanotechnol.* **2016**, *11*, 37–41. [CrossRef] [PubMed]
37. Maharjan, N.; Nakarmi, M.L. Luminescence properties of hexagonal boron nitride powders probed by deep UV photoluminescence spectroscopy. *MRS Adv.* **2021**, *6*, 307–310. [CrossRef] [PubMed]
38. Wang, Q.; Zhang, Q.; Zhao, X.; Luo, X.; Wong, C.P.Y.; Wang, J.; Wan, D.; Venkatesan, T.; Pennycook, S.J.; Loh, K.P.; et al. Photoluminescence Upconversion by Defects in Hexagonal Boron Nitride. *Nano Lett.* **2018**, *18*, 6898–6905. [CrossRef] [PubMed]
39. Zhu, J.; Li, D.; Chen, H.; Yang, X.; Lu, L.; Wang, X. Highly dispersed CuO nanoparticles prepared by a novel quick-precipitation method. *Mater. Lett.* **2004**, *58*, 3324–3327. [CrossRef]
40. Zhang, Y.X.; Kuang, M.; Wang, J.J. Mesoporous CuO–NiO micropolyhedrons: Facile synthesis, morphological evolution and pseudocapcitive performance. *CrystEngComm* **2014**, *16*, 492–498. [CrossRef]
41. Zhai, Y.; Ji, Y.; Wang, G.; Zhu, Y.; Liu, H.; Zhong, Z.; Su, F. Controllable wet synthesis of multicomponent copper-based catalysts for Rochow reaction. *RSC Adv.* **2015**, *5*, 73011–73019. [CrossRef]
42. Nath, A.; Shah, A.; Singh, L.R.; Mahato, M. Waste plastic-derived NiO-MWCNT composite as visible light photocatalyst for degradation of methylene blue dye. *Nanotechnol. Environ. Eng.* **2021**, *6*, 70. [CrossRef]

43. Kumar, S.; Bhawna; Gupta, A.; Kumar, R.; Bharti, A.; Kumar, A.; Kumar, V. New Insights into Cu/Cu_2O/CuO Nanocomposite Heterojunction Facilitating Photocatalytic Generation of Green Fuel and Detoxification of Organic Pollutants. *J. Phys. Chem. C* **2023**, *127*, 7095–7106. [CrossRef]
44. Jun, S.E.; Kim, Y.-H.; Kim, J.; Cheon, W.S.; Choi, S.; Yang, J.; Park, H.; Lee, H.; Park, S.H.; Kwon, K.C.; et al. Atomically dispersed iridium catalysts on silicon photoanode for efficient photoelectrochemical water splitting. *Nat. Commun.* **2023**, *14*, 609. [CrossRef] [PubMed]
45. Bojestig, E.; Cao, Y.; Nyborg, L. Surface chemical analysis of copper powder used in additive manufacturing. *Surf. Interface Anal.* **2020**, *52*, 1104–1110. [CrossRef]
46. Liu, Z.; Amiridis, M.D.; Chen, Y. Characterization of CuO Supported on Tetragonal ZrO_2 Catalysts for N_2O Decomposition to N_2. *J. Phys. Chem. B* **2005**, *109*, 1251–1255. [CrossRef] [PubMed]
47. Cheng, M.; Fan, H.; Song, Y.; Cui, Y.; Wang, R. Interconnected hierarchical $NiCo_2O_4$ microspheres as high-performance electrode materials for supercapacitors. *Dalton Trans.* **2017**, *46*, 9201–9209. [CrossRef] [PubMed]
48. Wang, H.; Zou, H.; Liu, Y.; Liu, Z.; Sun, W.; Lin, K.A.; Li, T.; Luo, S. Ni_2P nanocrystals embedded Ni-MOF nanosheets supported on nickel foam as bifunctional electrocatalyst for urea electrolysis. *Sci. Rep.* **2021**, *11*, 21414. [CrossRef] [PubMed]
49. Xue, H.; Meng, T.; Liu, F.; Guo, X.; Wang, S.; Mao, D. Enhanced resistance to calcium poisoning on Zr-modified Cu/ZSM-5 catalysts for the selective catalytic reduction of NO with NH_3. *RSC Adv.* **2019**, *9*, 38477–38485. [CrossRef] [PubMed]
50. Khan, W.U.; Chen, S.S.; Tsang, D.C.W.; Teoh, W.Y.; Hu, X.; Lam, F.L.Y.; Yip, A.C.K. Catalytically active interfaces in titania nanorod-supported copper catalysts for CO oxidation. *Nano Res.* **2020**, *13*, 533–542. [CrossRef]
51. Li, C.; Yang, Y.; Ren, W.; Wang, J.; Zhu, T.; Xu, W. Effect of Ce doping on catalytic performance of Cu/TiO_2 for CO oxidation. *Catal. Lett.* **2020**, *150*, 2045–2055. [CrossRef]
52. Yang, F.; Liu, D.; Zhao, Y.; Wang, H.; Han, J.; Ge, Q.; Zhu, X. Size Dependence of Vapor Phase Hydrodeoxygenation of m-Cresol on Ni/SiO_2 Catalysts. *ACS Catal.* **2018**, *8*, 1672–1682. [CrossRef]
53. Ma, Y.; Liu, J.; Chu, M.; Yue, J.; Cui, Y.; Xu, G. Cooperation Between Active Metal and Basic Support in Ni-Based Catalyst for Low-Temperature CO_2 Methanation. *Catal. Lett.* **2020**, *150*, 1418–1426. [CrossRef]
54. Wang, Z.; Zhou, F.; Lv, B.; Yu, J.; Zhang, J.; Zhang, Y.; Wu, Y.; Wang, Y.; Luo, W. Unveiling pH-Dependent Mechanistic Shifts in Cu_2O-Catalyzed Nitrate Electroreduction for Selective Ammonia Synthesis. *Adv. Sustain. Syst.* **2025**, *9*, e00211. [CrossRef]
55. Hu, B.; Liu, Y.; Zhou, Y.; Yang, S.; Wang, Z.; Tew, Y.S.; Shankar, H.; Wang, X.; Ou, P.; Wang, L. Electrosynthesis of urea on cadmium-modified iron oxide. *Nat. Synth.* **2026**, *5*, 885–896. [CrossRef]
56. Yao, Y.; Goodman, D.W. In situ IR spectroscopic studies of Ni surface segregation induced by CO adsorption on Cu–Ni/SiO_2 bimetallic catalysts. *Phys. Chem. Chem. Phys.* **2014**, *16*, 3823–3829. [CrossRef] [PubMed]
57. Shen, T.; Liu, S.; Yan, W.; Wang, J. Highly efficient preparation of hexagonal boron nitride by direct microwave heating for dye removal. *J. Mater. Sci.* **2019**, *54*, 8852–8859. [CrossRef]
58. Dubal, D.P.; Gund, G.S.; Lokhande, C.D.; Holze, R. CuO cauliflowers for supercapacitor application: Novel potentiodynamic deposition. *Mater. Res. Bull.* **2013**, *48*, 923–928. [CrossRef]

Disclaimer/Publisher's Note: The statements, opinions and data contained in all publications are solely those of the individual author(s) and contributor(s) and not of MDPI and/or the editor(s). MDPI and/or the editor(s) disclaim responsibility for any injury to people or property resulting from any ideas, methods, instructions or products referred to in the content.